Influence of laser processing of the low alloy medium carbon structural steel on the development of the fatigue crack

Marek Szkodo[1], Anna Bień[2],

[1] Mechanical Engineering Faculty, Gdansk University of Technology, Narutowicza 11/12, 80-233 Gdańsk, Poland, mszkodo@pg.gda.pl

[2] Technical Sciences Faculty, University of Warmia and Mazury in Olsztyn, Oczapowskiego 11, 10-719 Olsztyn, Poland, abien@uwm.edu.pl,

Abstract

The paper contains the results of the structural analysis, hardness tests and fatigue tests conducted for the medium carbon structural steel with low content of Cr and Ni after its processing with CO_2 laser beam. Pre-cracks were made in the round compact tension (RCT) specimen used for fatigue test. Next, four paths, parallel to each other, were melted on both sides of the samples using a laser beam. The paths were perpendicular to the direction of the axis of the cut notch. The first melted path ran at a distance of about 2.5 mm from the pre crack tip. Fatigue test results were compared with the sample which was not subjected to laser treatment. The fatigue tests showed that the sample with no laser treatment fractured after 270 000 cycles and the laser treated sample was able to withstand 7.2 million cycles for the same load and during this time the crack length increased only 0.4 mm. Hardness tests to estimate the residual internal stresses in the melted zone, in the heat affected zone (HAZ) and in the native material were carried out using nanointender. It was shown that compressive residual stress, in native material, close to HAZ in half-length of the melted path, just before the front of the crack, was 1165 MPa. These residual stresses contribute to the stopping of the development of the fatigue crack. It was also shown that the longitudinal manganese sulphide inclusions reduce crack development rate probably by blunting the crack blade.

Keywords: laser treatment; fatigue; low alloy steel; residual stress

1. Introduction

Lasers have been used in many fields since their invention. Lasers have also found applications in surface engineering. Cases of various materials can be modified by using a laser beam to give them other chemical, physical and mechanical properties. Laser treatment can improve, for example, the tribological properties [1-5], corrosion resistance of the surface layers [6-10] or significantly increase the surface hardness [11-14]. Using a laser beam, thermal stresses are generated in the surface layer during its heating [15]. For some materials, heating may also cause phase changes in the solid state which can further generate structural stress. Then the residual stresses are the sum of thermal and

structural stresses. Residual stresses can significantly affect the fatigue resistance of the processed material. If residual stresses are tensile, the fatigue strength decreases significantly. In the case of compressive stress, fatigue strength increases significantly since then it reduces the tensile stresses before the face of the fatigue crack. For example Wei and Ling [16] presented a three dimensional model to predict the development, magnitude and distribution of residual stress field induced by laser shock processing (LSP). They reached the conclusion that the overlap between two laser surface locations improves the magnitude and the affected depth of the residual stress. Morales et al also reported [17] that from the practical point of view, the LSP technology allows the effective induction of residual stresses fields in metallic materials. Cvetkovski et al showed in [18] that the development of residual stresses in medium carbon steels during their laser treatment depends on heating rate, temperature and mainly two material properties, thermal expansion/contraction and yield strength. In turn, Zhang et al studied the effect of two-sided laser heating of the aluminium 7050-T6 alloy on its fatigue resistance [19]. According to them, the laser treatment is very beneficial because crack initiation is delayed greatly, which plays a leading role in prolonging the fatigue life of specimen. Additionally crack propagation rate slows down which is attributed to superficial compressive residual stress induced by laser. Altus and Konstantino, in their work [20], enhanced fatigue resistance of Titanium 6Al–4V alloy using 1.8 kW continuous wave (CW) – CO_2 Laser. They attempted to find the optimal conditions of laser treatment which will improve the material resistance to fatigue failure, and explore the mechanisms involved. They identified two basic mechanisms. One is related to healing mechanism (HM), and the other is connected to microstructure mechanism (MM). Healing was found to be effective for surface temperatures above 400 °C. They reached a conclusion that the changes of microstructure adversely affect fatigue resistance except for temperatures lower than 600 °C and specific laser conditions. They also found a positive correlation between hardness and fatigue life. Bień also reported [21] the beneficial effects of selective laser re-melting of the steel on fatigue crack propagation. According to her research, the modification of the steel microstructure due to the laser beam re-melting increases fatigue strength of the processed materials.

This paper presents the possibility of stopping a fatigue crack by melting the material before its front, using a laser beam. Matching parameters of the laser beam and the appropriate arrangement of the re-melted paths, large compressive stresses able to stop the fatigue crack can occur before the face of the crack.

The aim of this paper is to check whether using laser beam is capable of generating high enough compressive residual stresses in the areas before the face of the crack (near the heat affected zone but still outside of the zone) able to stop the fatigue cracks in the treated steel.

2. Experimental procedure

2.1. Investigated material

Low-alloy steel with a content of 0.30% C was used for research. Chemical composition of testing steel is presented in Table 1. This steel is designed for quenching and tempering and it is designated for the most loaded parts of machines and engines, which require a very good plastic properties. This grade of steel is used, inter alia, in the aircraft industry. Round compact tensile (RCT) specimen for fatigue testing was made from steel after softening. Next six samples were hardened by quenching (heating up to 850 °C and cooling in oil) and then they were tempered in 300 °C. After tempering, the samples were cooled in oil. After heat treatment, the mechanical properties of the steel are as follows: tensile strength 1620 MPa, yield strength 1510 MPa, elongation 10%, reduction of area of the specimen 45%, toughness 48 J.

Table 1. Chemical composition of investigated steel

chemical composition wt%							
C	Mn	Si	P	S	Cu	Cr	Ni
0.30	1.15	1.10	0.030	0.025	0.25	1.05	1.65

2.2. Laser beam treatment

Five RCT samples were treated by laser beam after making pre-cracks in samples. The width W and the thickness B of the cylindrical shape RCT sample was 37 mm and 7 mm respectively. The surface roughness (Ra) of the samples was 0.32 µm. Pre-cracks have a length of a = 12.5 mm (see Fig. 1) from the axis of the holes in the sample. One sample was left untreated. This sample was used as a reference. Then on both sides of the samples, four paths parallel to each other were melted using laser beam. The distance from each path (Y) was 5 mm and tracks were perpendicular to the direction of the axis of the cut notch (see Fig. 1). The first track runs at a distance of about 2.5 mm from the pre crack tip (X=24 mm). The length of each path was approximately 40 mm (Z). The width of each melted path ranged from 1.2 to 1.5 mm and the width of HAZ ranged from 0.7 to 0.95 mm. Laser treatment was performed starting from the track closest to the tip crack ($P1$). Then, another path was melted without waiting for the sample to cool down. Subsequent paths were performed on the other side of the samples in the same order. Laser treated sample was located on a metal plate for faster cooling. The samples were treated by various parameters of the laser beam. This paper presents the results of the sample which showed the best resistance to fatigue crack growth. The laser processing parameters for this sample are presented in Table 2. Samples were coated by colloidal graphite before laser treatment in order to reduce the light reflection of the treated surfaces. The surface roughness of the

samples in the melted paths was much greater than 0.32 μm and it was not measured. Increased roughness of the surface after the laser treatment was not an obstacle in stopping the fatigue crack.
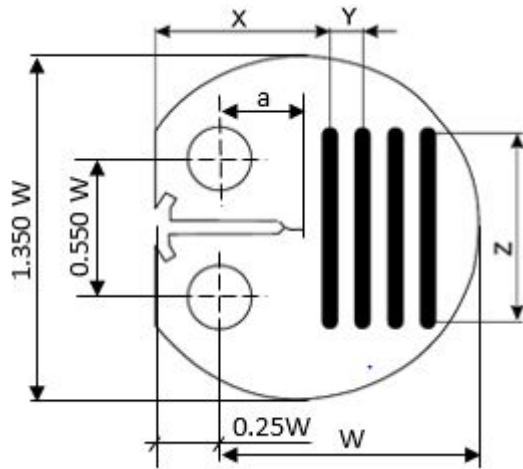

Fig. 1. RCT sample used for fatigue testing with marked melted paths. W - specimen width, X - distance from melted path to the front of the sample, Y – distance between melted paths, Z - length of melted path, a – length of the pre-crack

Table 2. Laser parameters used for melting of the sample

parameter	value
laser type	CO_2
laser mode	pulse
laser power [W]	$P = 840$
radius spot laser (the conversion) [mm]	$r = 1.6$
the speed of the laser beam [mm/s]	$v = 3.5$
shielding gas (low-pressure)	argon
the distance of the sample from the plane of the beam focusing lens [mm]	118
focal length of the lens ["]	3.8

2.3. Fatigue test

After laser processing, the resistance to fatigue crack propagation of laser treated sample was studied. The results were compared with the effects of fatigue tests carried out using the same parameters on the samples without the laser treatment. The results are the contents of the patent approved in 2012 [22]. The content of the patent describes the obtained effect without analyzing its reasons. Tests of crack propagation rate were performed on the testing machine MTS 8502 in the Air Force Institute of Technology in Warsaw. The maximum magnitude of the force was $F = 3500$ N. The frequency of the

load was 10 Hz with an asymmetry coefficient of the cycle $R = 0.2$. The temperature during the test was between 20-25 °C and air humidity 40% to 60%. The samples used in the fatigue tests were shaped as shown in Fig. 1 and had the following dimensions $W = 37$ mm and thickness $B = 7$ mm. Pre-cracks were made in the samples with a cyclic load at a frequency of 10 Hz and an asymmetry coefficient of the cycle equal to 0.1.

2.4. Material investigations

Fatigue fractures were examined using a scanning electron microscope (SEM, JOEL JSM-7800F) equipped with X-ray energy-dispersive spectroscopy. Structural investigations were carried out on parts of sample fracture with laser paths, within the melted tracks and between the tracks. Energy dispersive spectroscopy analysis (EDAX-TEAM™ EDS Analysis System) was performed in order to identify the precipitates in the microstructure. Transmission electron microscopy (TEM, JOEL JEM-1400Plus) was also used for structural examinations. Structural observations were carried out using the thin films. Microscopic examination was performed at the accelerating voltage of 45 kV. The hardness tests of the material were also performed after the fatigue investigation, using nanoindenter NanoTest Vantage. This test was performed to determine the qualitative and quantitative residual stresses in the melted paths, in the heat-affected zones (HAZ) and in the unprocessed materials. Qualitatively, the residual stresses were identified by the work of elastic deformation to be fixed in the hardness test. Quantitatively, the residual stresses were determined by the method described in the paper [23]. For this purpose, after the hardness test, the sample was subjected to stress relief annealing at 280 °C for 2 hours. Annealing was performed in a vacuum furnace. Hardness test was performed again after annealing, close to the same measurement points as before annealing. Residual stresses were calculated as the difference between the penetrator load for the sample with and without stress before and after annealing respectively, for the same depth of penetrator displacement, referred to the surface of the indentation for sample with residual stress. Hardness tests were performed, for a constant depth of penetration of the indenter equal to 5 μm. Berkovitch indenter was used for hardness investigations. Loading and unloading rates were 50 mN/s. Indentation contains one cycle with 5 s dwell at maximum load. Hardness tests were performed only for the laser treated sample. These tests were made along two lines (l1 and l3). Line l1 was 1 mm from the edge of fracture (approximately along the front of the crack) and the line l3 was at a distance of 10 mm (see Fig. 2). During the hardness tests, measurement system read the depth of the indenter displacement and transformed it into the hardness. Assuming that the stiffness of the frame is a linear function of the load of the indenter, the change in temperature of the measurement of hardness by ± 0.05 °C causes an error in reading the indenter displacement of about ± 4 nm. Because the temperature during the

hardness test was 21 °C ± 0.5 °C, the depth of indenter displacement was read with the accuracy of ± 40 nm. The displacement of the indenter was about 4000 nm, thus the hardness measurement accuracy was about 1%.

3. Results and discussion

Fig. 3 shows the changes of crack length versus the number of cycles. Both graphs are presented separately and in different scales in order to better illustrate the change in the rate of crack propagation. The sample with no laser treatment fractured after 270 000 of cycles at the crack length of 31.35 mm. The laser treated sample was able to withstand 7.2 million cycles at the same load and during this time the crack length increased only 0.4 mm. Because after the 7.2 million cycles the laser treated sample was not destroyed, the test was discontinued. Described effect occurred only for a specific, narrow range of laser beam parameters.
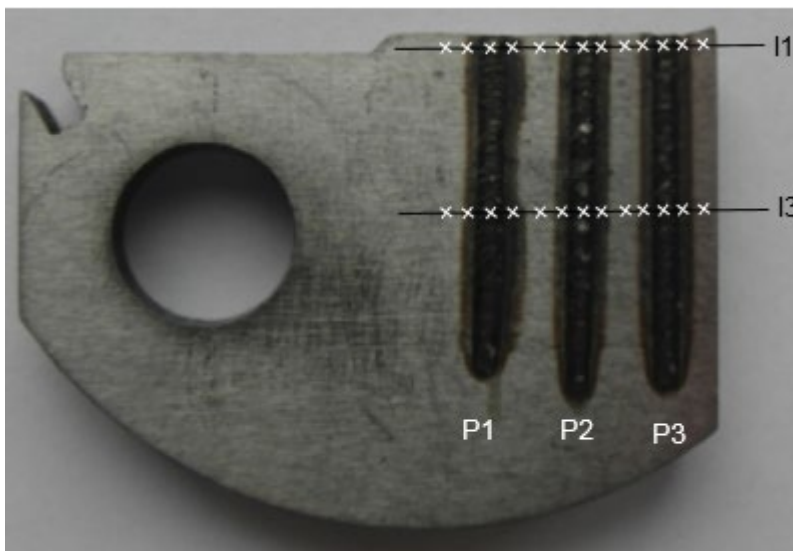

Fig. 2. View of the broken RCT specimen with the marked lines l1 and l3 along which the hardness measurements were performed. Marked crosses indicate the place of hardness measurement

Next, structural examinations were performed in order to verify the microstructural changes caused by the laser treatment. For this purpose the sample was broken after the applied static load. Fig. 4 shows the fracture of the laser melted path. There are different zones at the fracture: hardening from the liquid state zone, hardening from the solid state zone, the transition zone and the core. Structural examination of the fracture revealed that the laser treatment led to melting of the surface layer to a depth of about 200 μm (see Fig. 4). The direction of crystallization is evident
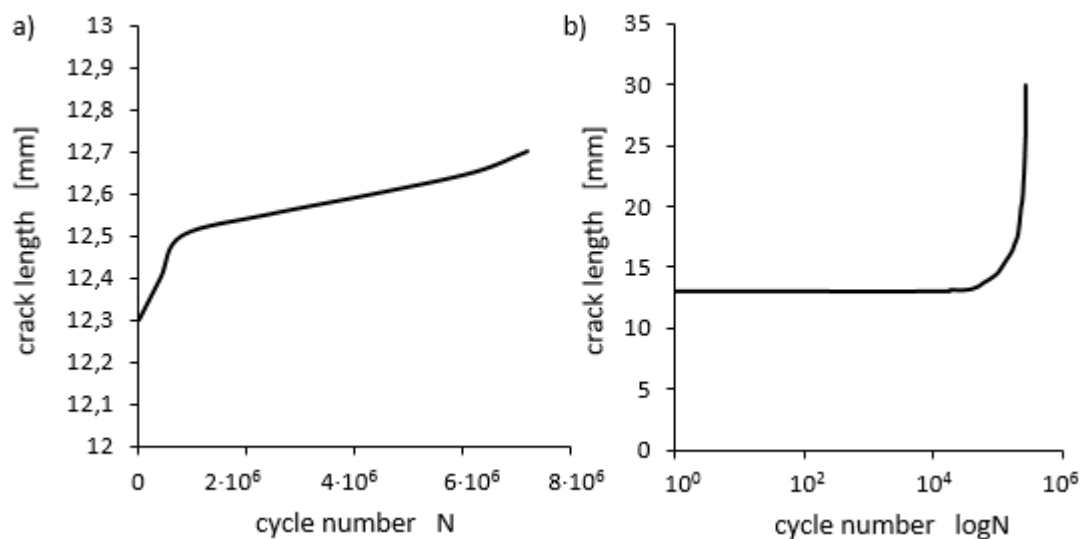
Fig. 3. Changes of the crack length vs. time for the sample after laser treatment – Fig. a) and for base material – Fig. b)

in the quenching from the liquid zone (see Fig. 5). Analyzing the microstructure of the fracture, it can
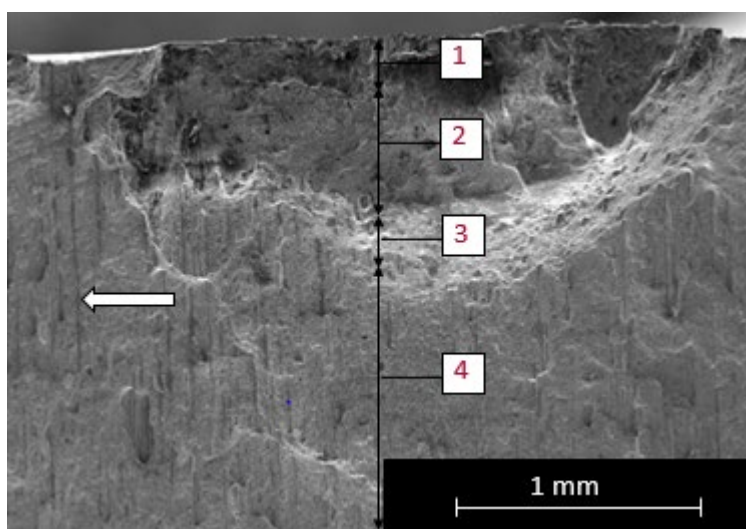

Fig. 4. Fracture of the broken sample after fatigue test. Different zones caused by the laser treatment can be seen at the fracture. Numerous, longitudinal non-metallic inclusions are located in unprocessed material (depicted by the arrow) (SEM). 1 - hardening from the liquid state zone, 2 -hardening from the solid state zone, 3 - the transition zone, 4 - the core
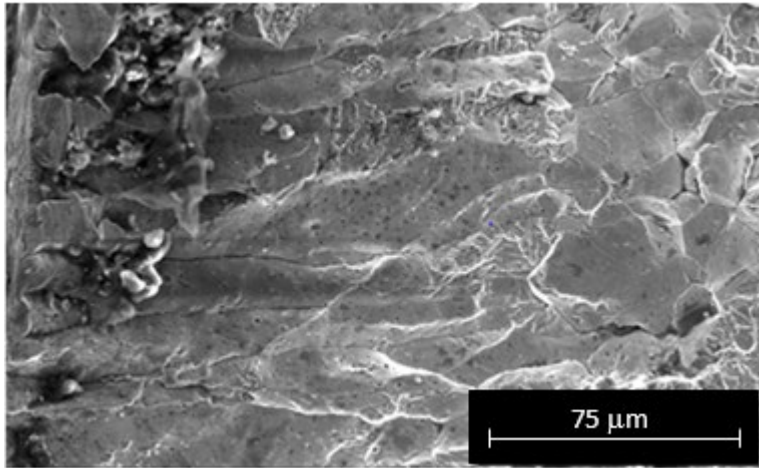
Fig. 5. Microstructure of a brittle fracture hardened from liquid state (SEM). The directed crystallization and spherical nonmetallic inclusions and carbides are visible

be concluded that there is an evident change in the fracture mechanism of the sample depending on the zone. The melted material, HAZ and transition zone revealed brittle fracture and unprocessed material showed ductile fracture (see Figs 5-6). Numerous longitudinal non-metallic inclusions are located in unprocessed material. Their arrangement was perpendicular to the direction of the crack propagation. EDS analysis showed that they are manganese sulphides. TEM investigations showed the presence of martensite in the melted zone. The presence of elements such as aluminum, sulfur, magnesium, oxygen and chromium was disclosed in melted zone in the result of EDS analysis. It is therefore assumed that the spherical separations occurring in the melted material are manganese sulphides, carbides and oxides (Fig 7). However, changes in the steel microstructure due to the laser
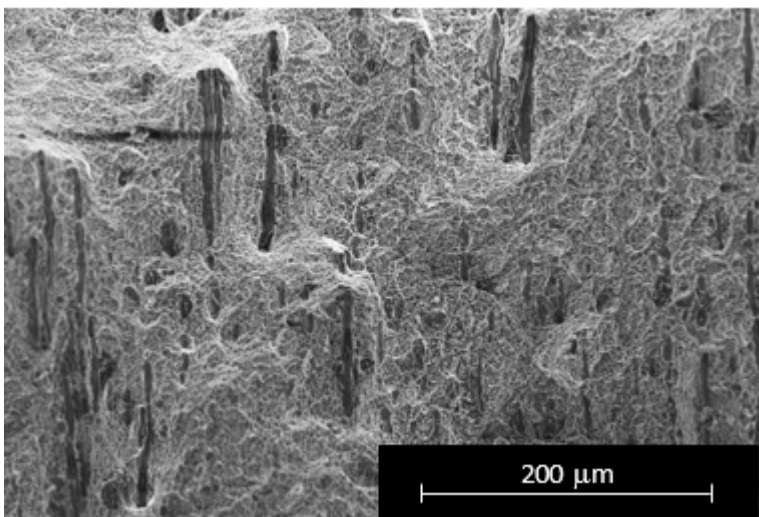

Fig. 6. Microstructure of a ductile fracture in the unprocessed material (SEM). Longitudinal manganese sulfides arranged perpendicularly to the direction of crack development are visible
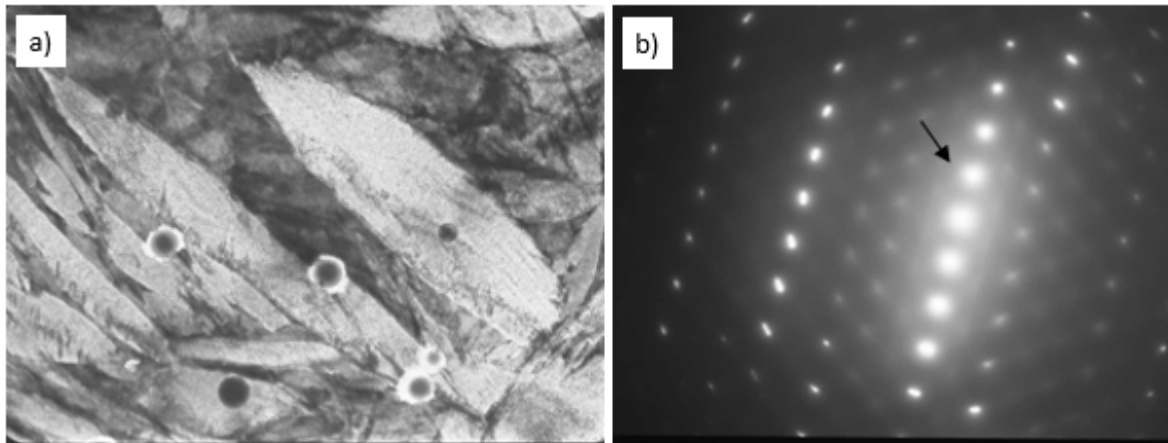
Fig. 7. The microstructure of steel melted by laser beam (TEM). Martensite with a large number of fine spheroidal manganese sulphides and carbides is visible – Fig. a). Diffraction pattern of microstructure presented in Fig. a. Blurry reflections evidence a high density of crystallographic defects in the microstructure – Fig. b)

treatment cannot explain the stopping crack propagation during fatigue test. In fact, stopping the development of crack occurred in the material area outside of the melted path and HAZ. The fatigue crack was blocked in areas of the unchanged microstructure and therefore the effect of microstructure on crack growth was not analyzed. Analysis of the microstructure obtained by the laser treatment was performed in order to find a correlation between the depth of melted material and the value of the stress generated in the base material just before the fatigue crack. In order to explain the reason for the crack stopping, micro-hardness tests along two lines (l1 and l3) were performed (see Fig. 2). Fig. 8 presents the results of micro-hardness test. As is apparent from Fig. 8, the measured hardness along l1 and l3 line is similar. However, the hardness in the HAZ is much higher for P2 and P3 paths at a distance of 1 mm from the edge of the fracture than the hardness in the same areas at a distance of 10 mm from the fracture edge. For the P1 path that was the closest to the front of the crack, hardness of the native material (NM), HAZ and laser melted (LM) steel were similar and lie
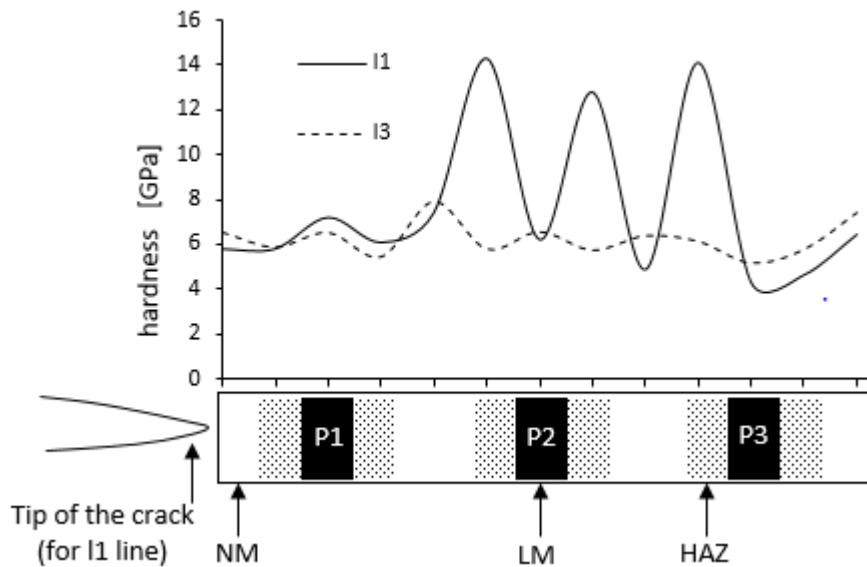
Fig. 8. The hardness at a distance of 1 mm (l1) and 10 mm (l3) from the edge of the fracture measured at a constant depth of 5 µm (NM – native material, LM – laser melted, HAZ – heat affected zone). The measurement points are shown in Fig. 2

within 6 - 8 GPa. For this path, described dependency occurred for both l1 and l3 lines. During the hardness test, plastic and elastic work of deformation of the tested material were also measured (Fig. 9). The portion of elastic work W_{el} (defined as in Fig. 10) relative to the total work of deformation can be a qualitative indicator of the residual stress. Fig. 9 shows the change in the elastic deformation
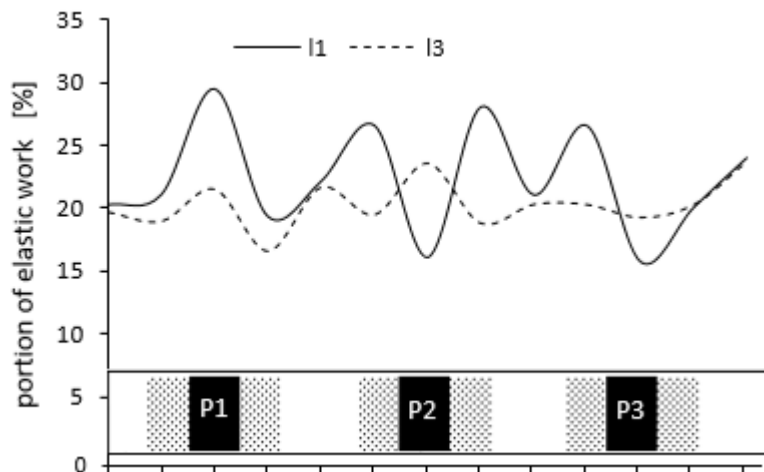

Fig. 9. Portion of elastic work relative to the total work of deformation for different areas of the sample. The measurement points are shown in Fig. 2

work for different areas of the sample. As is apparent from Fig. 9, the residual stress changes depend on the area of the sample. Residual stress increases up to the melted path P1 in the areas closest to the front of the crack (along l1 line). Another situation occurs along the l3 line. The residual stress in the native material proximate to the tip crack is higher than residual stress in HAZ, then it increases (in

the melted path) and next the residual stress decreases again (in HAZ on the other side of the P1 path). The differences in the course of changes of the portion of elastic work deformation along l1 and l3 lines indicate the generation of different residual stress along melted paths. In order to measure the residual stress values the sample was annealed and hardness test was done again. Figs. 10-11 present the examples of the changes of the load as a function of depth penetrator during
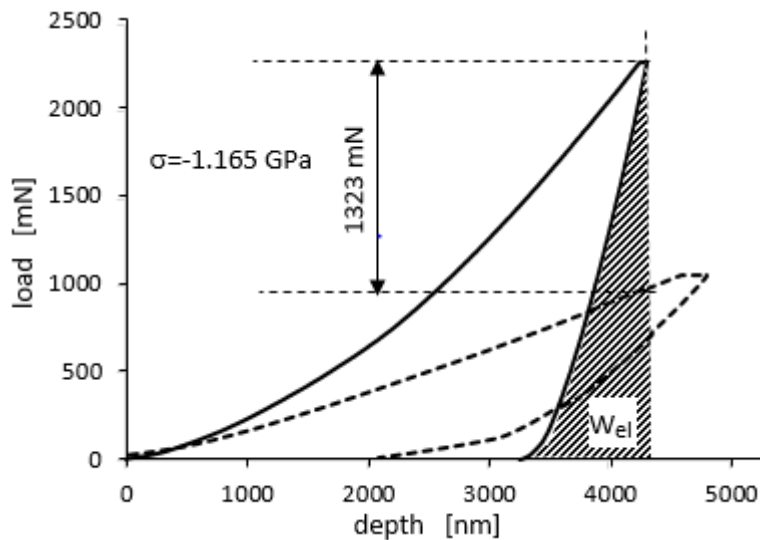

Fig. 10. Load vs. penetrator displacement during hardness measurement in l1 line in the native material in front of the crack tip. Solid line - for material with stress and dashed line – for material after annealing. Calculated compressive stress is 1.165 GPa

loading and unloading when measuring the hardness. If the load required for the penetrator displacement, at the same depth, is greater for the material with residual stress that means that the stress is compressive, as presented in the Fig. 10. If the situation is opposite it means that the stress is tensile, as in Fig 11. Calculated stresses are shown in Fig. 12. The most important for the retention of crack development were stresses along the l1 line in the vicinity of the crack tip. All calculated stresses along the l1 line were compressive stresses. Residual stresses were generally larger along the l1 line than l3 line. They equalize in the vicinity of the P3 path. Residual stress in the native material in front of the crack was 1165 MPa for l1 line (see Fig. 10). Compressive stress was even greater further away from the crack tip. Compressive stress reached a 1688 MPa value in HAZ of P1 path from the side of crack. In contrast, the residual stress in the native material from the side of the tip crack was 723 MPa at a distance of 10 mm from the edge of the fracture. Compressive stresses were smaller the further away from the crack tip, and in the HAZ they have changed the character.
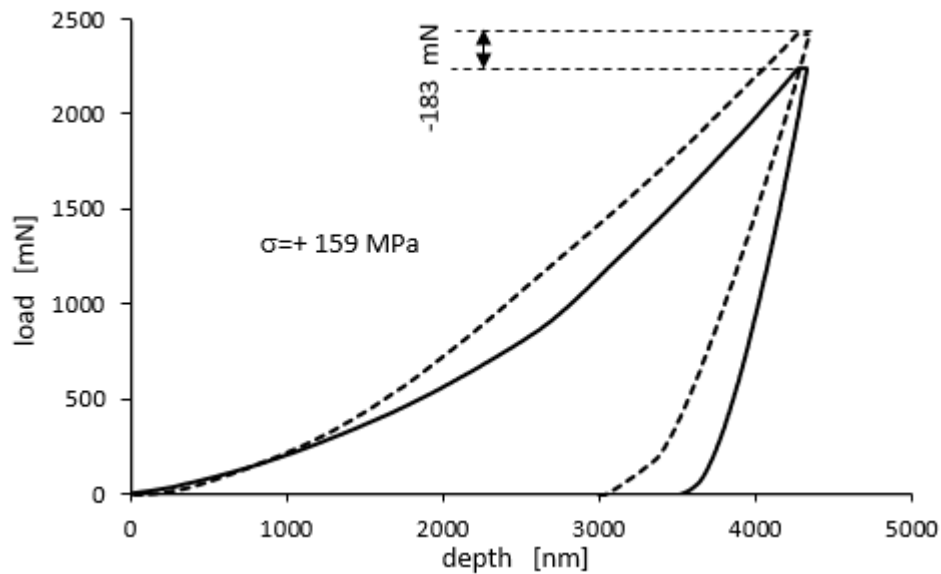
Fig. 11. Load vs. penetrator displacement during hardness measurement in l3 line in the HAZ of P1 path from the side of the crack. Solid line - for material with stress and dashed line – for material after annealing. Calculated tensile stress is 159 GPa
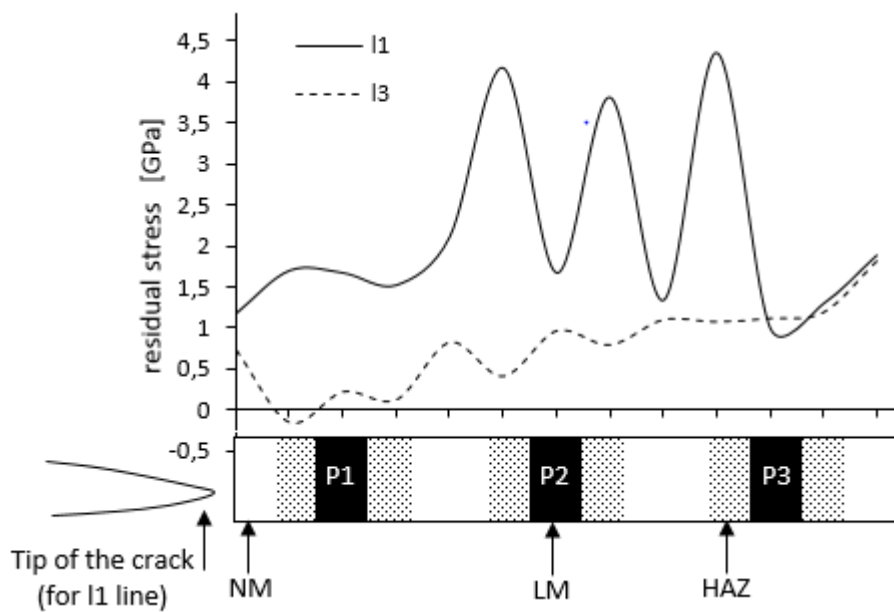

Fig. 12. Residual stress distribution along the l1 and l3 lines. The measurement points are shown in Fig. 2

Tensile stresses occurred in HAZ of P1 path from the side of crack, at a distance of 10 mm from the edge of the fracture. Their value reached 159 MPa (see Figs. 11 and 12). Residual stresses generated in the melted material and in the heat-affected zones of paths were the result of both phase transitions and temperature differences in the cross section of the sample and different cooling rate after the laser treatment. These stresses added together gave the resultant value as in the Fig. 12. While the residual stresses generated in the areas of structurally unchanged material (in native material) had

only the features of thermal stress. Residual stress value along l1 line ranged from 1 GPa to 2 GPa in areas where there were no structural changes, that is in areas between melted paths and between the first path and the crack. The value of thermal stress depends on many factors, inter alia, on the rate of heating and cooling, the heat conductivity, or the order of heating specific areas. But the biggest residual stresses occurred in the heat-affected zones of P1 and P2 paths. The stress reached a value of about 4 GPa in these areas. The analysis of the stress state at the tip of the crack was done, considering the stress distribution near its front. The stresses in the sample, without taking into account the stress concentration due to the crack occurrence, can be described by the equation:

$$\sigma = \sigma_t + \sigma_b = F/(L \cdot B) + 6(F \cdot x)/(B \cdot L^2) \tag{1}$$

Were:

σ_t – tensile stress

σ_b – bending stress

B – thickness of the sample (7 mm)
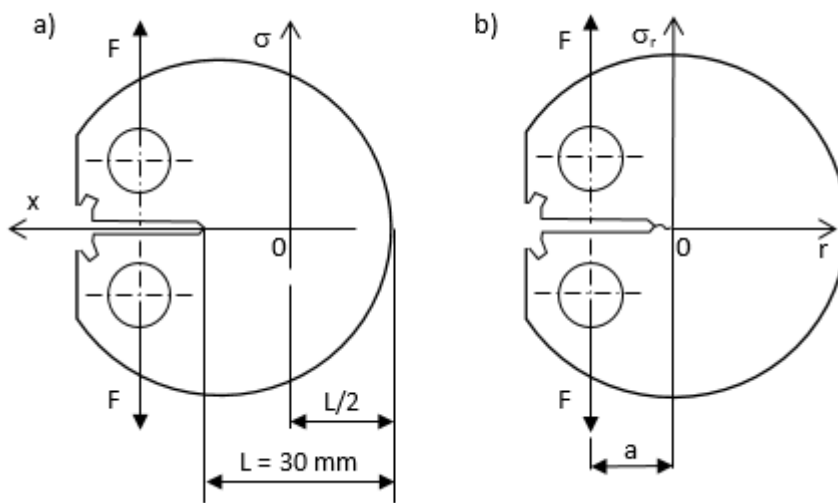
L – length 30 mm (see Fig. 13a)

Fig. 13. View of the sample with the selected dimensions to determine the stress $\sigma = f(x)$ – Fig. a) and $\sigma_r = f(r)$ – Fig. b)

Considering the occurrence of crack in the sample, the equation describing stress concentration before the tip of the crack can be written as:

$$\sigma_r = \sigma \left(1 + \sqrt{\frac{a}{2r}}\right) \tag{2}$$

Where:

σ_r – concentrated tensile stress caused by crack

r – distance from the tip of the crack

a – crack length (see Fig. 13b)

In Fig. 14, the dashed line shows the change in stress, without taking into account the stress concentration due to the crack. The maximum tensile stress occurs before the face of the crack, and its value is 683 MPa. The occurrence of crack causes stress concentrations that, theoretically, just before its forehead attain very high values (see equation 2). Solid line shows the concentrated stress
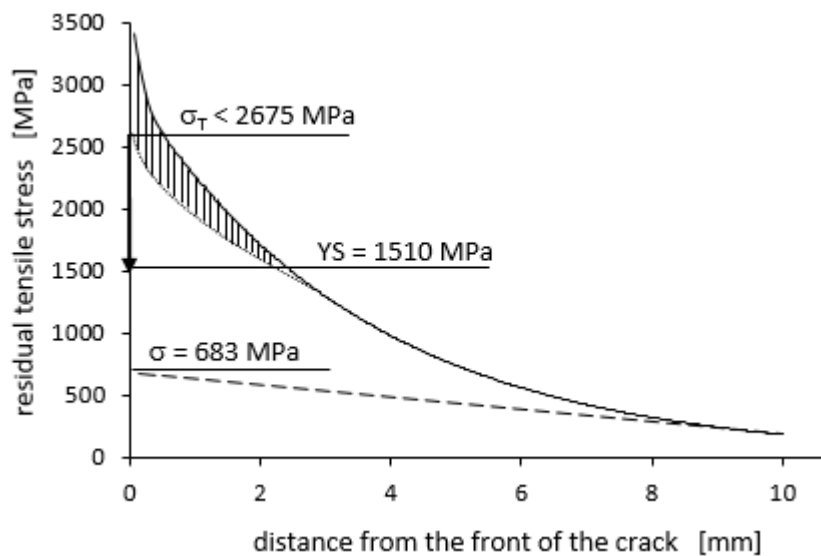

Fig. 14. Stress distribution before tip of the crack in the laser-treated sample during the fatigue test

distribution in Fig. 14. However, since the crack was not developed during the fatigue test, it can be assumed that just before the crack tip, the stress did not exceed the yield strength of the material. Reduction of the tensile stress before the face of the crack was caused by two factors. The first reason was the presence of the elongated manganese sulfides inclusions in the steel arranged perpendicularly to the direction of developing crack (see Fig. 4). The presence of manganese sulfides caused blunting of blade of the crack, which resulted in a decrease in tensile stress before its face. The phenomenon of blunting of the blade of the crack and related decrease in tensile stress before its face is reflected by the shaded area in Fig. 14. Such an assumption is confirmed by the course of the crack development (see Fig. 3a). As is apparent from Fig. 3a the crack development rate is higher in the first period fatigue test (to about 350,000 cycles). After this first period, the crack development rate decreased. Reduction of the crack development rate was probably caused by blunting of the crack blade due to the occurrence of longitudinal manganese sulfide and other non-metallic inclusions. The second reason causing the stopping of the crack during the fatigue test was the occurrence of the compressive stress (σ_C = 1165 MPa) in front of its face induced by the laser treatment. The reduction of tensile stress before the front of the crack, due to laser treatment, is illustrated by the arrow in Fig. 14. Both of these factors resulted in a reduction in tensile stress before the face of the crack, below yield strength (YS)

of the steel. Since the yield strength of the steel was 1510 MPa and the compressive stress (σ_C) before the face of the crack caused by the laser treatment amounted to 1165 MPa, the stress before the tip of the crack (σ_T) can be readily calculated from the relation:

$\sigma_T - \sigma_C < YS$ from this it follows that $\sigma_T < YS + \sigma_C$ it is $\sigma_T < 1510 + 1165$, $\sigma_T < 2675$ MPa

Laser treatment has been made on both sides of the sample and one can assume that there were the same residual stresses on the other side as well. The measured residual stresses related only to a depth of about 5 μm and do not provide information about their values throughout the whole cross-section of the sample. But the stopping of crack development can attest to the fact that large compressive stresses were also generated at greater depths.

Stress before the face of crack for the reference sample without laser treatment was about 2600 MPa and substantially exceed the yield strength of steel which resulted in the rapid development of fatigue crack.

The fatigue crack was blocked in areas of the unchanged microstructure and therefore the effect of microstructure on crack growth was not analyzed. Analysis of the microstructure obtained by the laser treatment was performed in order to find a correlation between the depth of melted material and the value of the stress generated in the base material just before the fatigue crack. The highest compressive stress generated in the base material just before the fatigue crack was obtained after melting, at about 200 μm. Larger or smaller depth of re-melting or hardening of the material from the solid state did not provide sufficiently large compressive stress values able to block the development of a fatigue crack.

4. Conclusion

Round Compact Tensile specimen was melted on multiple paths using a CO_2 laser beam and then subjected to fatigue test. The paths were perpendicular to the direction of the axis of the cut notch. Fatigue test results were compared with the sample which was not subjected to laser treatment. In order to determine the level of the residual stress in melted paths, in HAZ and in the native material caused by a laser treatment, hardness tests were made by using nanoindenter. Also, structural investigations were carried out on parts of the sample fracture with laser paths, within the melted tracks and between the tracks. The obtained results allow forming the following conclusions:

1. The fatigue tests showed that the sample with no laser treatment fractured after 270 000 cycles and the laser treated sample was able to withstand 7.2 million cycles for the same load.

2. By applying the laser treatment to, the native material i.e. outside the melted steel and heat affected zone it is possible to generate high enough residual compressive thermal stress, ~~without structural changes~~ capable of stopping the fatigue cracks. Its value was 1.165 GPa in the vicinity of the crack tip.

3. In the described experiment, the parameters used in the laser treatment allowed to generate the greatest compressive stress in the half-length of melted paths.

4. The highest levels of the residual stress were in HAZ. Their values were up to 4 GPa.

5. The hardness and volume residual stresses in the middle of the melted paths correspond well to each other.

6. Presence of manganese sulfide inclusions in the metal matrix of native material, whose arrangement was perpendicular to the direction of the fatigue crack propagation, substantially contributes to reduction of tensile stresses before the face of the crack probably by blunting the crack blade.

References

[1] J.M. Vázquez-Martínez, J. Salguero, F.J. Botana, J.P. Contreras, S.R. Fernández-Vidal, M. Marcos. Procedia Engineering. 63 (2013) 752-60.

[2] Y. Qin, D. Xiong, J. Li. Tribological properties of laser surface textured and plasma electrolytic oxidation duplex-treated Ti6Al4V alloy deposited with MoS2 film. Surface and Coatings Technology. 269 (2015) 266-72.

[3] M. Kulka, P. Dziarski, N. Makuch, A. Piasecki, A. Miklaszewski. Microstructure and properties of laser-borided Inconel 600-alloy. Applied Surface Science. 284 (2013) 757-71.

[4] M. Pellizzari, M.G. De Flora. Influence of laser hardening on the tribological properties of forged steel for hot rolls. Wear. 271 (2011) 2402-11.

[5] M. Hashim, K.E. Sarath Raghavendra Babu, M. Duraiselvam, H. Natu. Improvement of wear resistance of Hastelloy C-276 through laser surface melting. Materials & Design. 46 (2013) 546-51.

[6] B.S. Yilbas, I. Toor, C. Karatas, J. Malik, I. Ovali. Laser treatment of dual matrix structured cast iron surface: Corrosion resistance of surface. Optics and Lasers in Engineering. 64 (2015) 17-22.

[7] B.S. Yilbas, I.-u.-H. Toor, J. Malik, F. Patel. Laser gas assisted treatment of AISI H12 tool steel and corrosion properties. Optics and Lasers in Engineering. 54 (2014) 8-13.

[8] H. Liu, C. Wang, X. Zhang, Y. Jiang, C. Cai, S. Tang. Improving the corrosion resistance and mechanical property of 45 steel surface by laser cladding with Ni60CuMoW alloy powder. Surface and Coatings Technology. 228, Supplement 1 (2013) S296-S300.

[9] R. Cottam, M. Brandt, J.L.G. Waugh, 20 - Laser surface treatment to improve the surface corrosion properties of nickel-aluminum bronze, Laser Surface Engineering, Woodhead Publishing, 2015, pp. 469-81.

[10] M.M. Pariona, V. Teleginski, K.d. Santos, S. Machado, A.J. Zara, N.K. Zurba, et al. Yb-fiber laser beam effects on the surface modification of Al–Fe aerospace alloy obtaining weld filet structures, low fine porosity and corrosion resistance. Surface and Coatings Technology. 206 (2012) 2293-301.

[11] H.C. Man, M. Bai, F.T. Cheng. Laser diffusion nitriding of Ti–6Al–4V for improving hardness and wear resistance. Applied Surface Science. 258 (2011) 436-41.

[12] C. Soriano, J. Leunda, J. Lambarri, V. García Navas, C. Sanz. Effect of laser surface hardening on the microstructure, hardness and residual stresses of austempered ductile iron grades. Applied Surface Science. 257 (2011) 7101-6.

[13] S.J. Hindus, S.H. Kumar, S.X. Arockiyaraj, M.V. Kannan, P. Kuppan. Experimental Investigation on Laser Assisted Surface Tempering of AISI D2 Tool Steel. Procedia Engineering. 97 (2014) 1489-95.

[14] A. Bień, M. Szkodo. Surface treatment of C80U steel by long CO2 laser pulses. Journal of Materials Processing Technology. 217 (2015) 114-21.

[15] B.S. Yilbas, A. Matthews, A. Leyland, C. Karatas, S.S. Akhtar, B.J. Abdul Aleem. Laser surface modification treatment of aluminum bronze with B4C. Applied Surface Science. 263 (2012) 804-9.

[16] X.L. Wei, X. Ling. Numerical modeling of residual stress induced by laser shock processing. Applied Surface Science. 301 (2014) 557-63.

[17] M. Morales, J.L. Ocaña, C. Molpeceres, J.A. Porro, A. García-Beltrán. Model based optimization criteria for the generation of deep compressive residual stress fields in high elastic limit metallic alloys by ns-laser shock processing. Surface and Coatings Technology. 202 (2008) 2257-62.

[18] K. Cvetkovski, J. Ahlström, B. Karlsson. Influence of short heat pulses on properties of martensite in medium carbon steels. Materials Science and Engineering: A. 561 (2013) 321-8.

[19] X.Q. Zhang, H. Li, X.L. Yu, Y. Zhou, S.W. Duan, S.Z. Li, et al. Investigation on effect of laser shock processing on fatigue crack initiation and its growth in aluminum alloy plate. Materials & Design. 65 (2015) 425-31.

[20] E. Altus, E. Konstantino. Optimum laser surface treatment of fatigue damaged Ti–6Al–4V alloy. Materials Science and Engineering: A. 302 (2001) 100-5.

[21] A. Bień. Laser surface modification of metal alloys and its effect on the fatigue crack propagation in terms of the microstructure (in Polish). UWM, 2013.

[22] A. Bień, S. Kłysz, Method to block the propagation of fatigue cracks (in Polish), in: P.C.f. Standardization (Ed.), Poland, 2012.

[23] Y.-H. Lee, D. Kwon. Residual stresses in DLC/Si and Au/Si systems: Application of a stress relaxation model to the nanoindentation technique. Journal of Materials Research. 17 (2002) 901-6.

Figure captions

Fig. 1. RCT sample used for fatigue testing with marked melted paths. W - specimen width, X - distance from melted path to the front of the sample, Y – distance between melted paths, Z - length of melted path, a – length of the pre-crack

Fig. 2. View of the broken RCT specimen with the marked lines l1 and l3 along which the hardness measurements were performed. Marked crosses indicate the place of hardness measurement

Fig. 3. Changes of the crack length vs. time for the sample after laser treatment – Fig. a) and for base material – Fig. b)

Fig. 4. Fracture of the broken sample after fatigue test. Different zones caused by the laser treatment can be seen at the fracture. Numerous, longitudinal non-metallic inclusions are located in unprocessed material (depicted by the arrow) (SEM). 1 - hardening from the liquid state zone, 2 -hardening from the solid state zone, 3 - the transition zone, 4 - the core

Fig. 5. Microstructure of a brittle fracture hardened from liquid state (SEM). The directed crystallization and spherical nonmetallic inclusions and carbides are visible

Fig. 6. Microstructure of a ductile fracture in the unprocessed material (SEM). Longitudinal manganese sulfides arranged perpendicularly to the direction of crack development are visible

Fig. 7. The microstructure of steel melted by laser beam (TEM). Martensite with a large number of fine spheroidal manganese sulphides and carbides is visible – Fig. a). Diffraction pattern of microstructure presented in Fig. a. Blurry reflections evidence a high density of crystallographic defects in the microstructure – Fig. b)

Fig. 8. The hardness at a distance of 1 mm (l1) and 10 mm (l3) from the edge of the fracture measured at a constant depth of 5 µm (NM – native material, LM – laser melted, HAZ – heat affected zone). The measurement points are shown in Fig. 2

Fig. 9. Portion of elastic work relative to the total work of deformation for different areas of the sample. The measurement points are shown in Fig. 2

Fig. 10. Load vs. penetrator displacement during hardness measurement in l1 line in the native material in front of the crack tip. Solid line - for material with stress and dashed line – for material after annealing. Calculated compressive stress is 1.165 GPa

Fig. 11. Load vs. penetrator displacement during hardness measurement in l3 line in the HAZ of P1 path from the side of the crack. Solid line - for material with stress and dashed line – for material after annealing. Calculated tensile stress is 159 GPa

Fig. 12. Residual stress distribution along the l1 and l3 lines. The measurement points are shown in Fig. 2

Fig. 13. View of the sample with the selected dimensions to determine the stress $\sigma = f(x)$ – Fig. a) and $\sigma_r = f(r)$ – Fig. b)

Fig. 14. Stress distribution before tip of the crack in the laser-treated sample during the fatigue test